The Influence of Out-of-Plane Geometry on Pulsatile Flow within a Distal End-To-Side Anastomosis

Y. Papaharilaou[1,2], D.J. Doorly[1], S.J. Sherwin[1]

[1]Biomedical Flow Group,
Aeronautics Department,
Imperial College of Science, Technology and Medicine
Prince Consort Road,
London, SW7 2BY, United Kingdom.

[2]Department of Biological and Medical Systems
Imperial College of Science, Technology and Medicine
Exhibition Road,
London SW7 2BX, United Kingdom

Keywords: Bypass grafts, Out-of-plane geometry, Hemodynamics, Computational Fluid Dynamics, Magnetic Resonance Imaging of flow

Corresponding Author:
D.J. Doorly,
Tel: 0044-20-75945049
Fax: 0044-20-75848120
e-mail: d.doorly@ic.ac.uk

Reprint Address:
D.J. Doorly,
Aeronautics Department,
Imperial College,
London, SW7 2BY, United Kingdom.

Manuscript submitted to the *Journal of Biomechanics* 16 June 2001.

Revised 18 February 2002

ABSTRACT

We present an experimental and computational investigation of time-varying flow in an idealised fully occluded 45-degree distal end-to-side anastomosis. Two geometric configurations are assessed, one where the centrelines of host and bypass vessels lie within a plane, and one where the bypass vessel is deformed out of the plane of symmetry, respectively termed planar and non-planar. Flow experiments were conducted by magnetic resonance imaging in rigid wall models and computations were performed using a high order spectral/hp algorithm. Results indicate a significant change in the spatial distribution of wall shear stress and a reduction of the time-averaged peak wall shear stress magnitude by 10 % in the non-planar model as compared to the planar configuration. In the planar geometry the stagnation point follows a straight-line path along the host artery bed with a path length of 0.8 diameters. By contrast in the non-planar case the stagnation point oscillates about a centre that is located off the symmetry plane intersection with the host artery bed wall, and follows a parabolic path with a 0.7 diameter longitudinal and 0.5 diameter transverse excursion. A definition of the oscillatory shear index (OSI) is introduced that varies between 0 and 0.5 and that accounts for a continuous range of wall shear stress vector angles. In both models, regions of elevated oscillatory shear were spatially associated with regions of separated or oscillating stagnation point flow. The mean oscillatory shear magnitude (considering sites where OSI>0.1) in the non-planar geometry was reduced by 22 % as compared to the planar configuration. These changes in the dynamic behaviour of the stagnation point and the oscillatory shear distribution introduced by out-of-plane graft curvature may influence the localisation of vessel wall sites exposed to physiologically unfavorable flow conditions.

1. Introduction

A large number of arterial bypass grafts are implanted annually, worldwide, to relieve arterial occlusion. However, up to 25% fail by 1 year and up to 50% by 10 years (Bryan and Angelini, 1994; Cheshire and Wolfe, 1993). The principal cause of arterial bypass graft failure is stenosis secondary to intimal hyperplasia. It is well known that a strong link between vessel wall biology and the local flow field exists with wall shear stress being one of the most influential flow features (Davies, 1995). Although the exact mechanisms associated with the development of vessel wall disease have not been fully understood, it has been demonstrated that intimal hyperplasia tends to occur preferentially in regions of low time averaged shear stress and long residence times (Ohja et al., 1990; Sottiurai et al., 1989; Bassiouny et al., 1992). It has also been suggested that a link exists between spatial wall shear stress gradients or rapid temporal changes in wall shear stress and regions where intimal hyperplasia preferentially develops (Ohja et al., 1990; Ohja, 1993; Lei et al., 1997).

Local flow features such as low time averaged shear, flow separation and shear oscillation have been found to promote the development of atherosclerotic lesions (Ku and Giddens, 1983; Friedman et al., 1987; Yamamoto et al., 1992). Furthermore a correlation has been found (Asakura and Karino, 1990) between regions of low wall shear stress and flow recirculation and locations of atheroma in fixed coronary arteries.

Although there has been extensive research on the effect of hemodynamics on vessel pathogenesis (Lei et al., 2001; Steinman et al., 1996; Hofer et al., 1996; Henry et al., 1996; White et al., 1993; Sottiurai et al., 1989; Ohja et al., 1990; Ohja, 1993), little work has been done to investigate the effects of the three-dimensional nature of the geometry of the vessels (Caro et al., 1996; Sherwin et al., 1997; Ding and Friedman, 1997) such geometry would be found in a physiologically correct anastomosis. So far most investigations whether *in vitro* experimental or numerical simulations have been restricted to geometries where the bypass and host vessel centerlines lie in a plane and can be termed planar. A few studies (Sherwin et al., 2000; Xu et al., 1999; Moore et al., 1999) investigated model geometries with out-of-plane curvature. Moore et al. (1999) removed geometrical features from an anatomically faithful finite element model of a human end-to-side arterial anastomosis to produce a series of simplified models. They reported that removal of out-of-plane curvature substantially changed the secondary flow field and particle residence times, but did not markedly alter the distribution of wall shear stress. However, they considered only models with a hood, which by expanding graft cross-sectional area and reducing mean velocity, would potentially lessen the effect of out-of-plane curvature on the flow field.

Sherwin et al. (2000) compared steady flow features from two distal anastomosis geometries, one planar and one non-planar. In the non-planar configuration the bypass vessel lies perpendicular to the original planar geometry as shown in Fig. 1. The planar geometry used includes a 45^{O} anastomosis

and the host vessel is fully occluded proximal to the anastomotic junction similar to previous investigations (Steinman et al., 1996; Hofer et al., 1996; Henry et al., 1996; Ethier et al., 2000). In a study by Ethier et al. (1998) on the planar end-to-side anastomosis the significance of the effects of flow pulsatility on the flow patterns and the wall shear stress distribution was demonstrated.

The aim of this investigation is to achieve fundamental understanding of the influence of out-of-plane curvature in the graft in a controlled and well-studied transient flow environment. This objective would not have been met as part of a patient specific study. We further the investigations of Sherwin et al. (2000) by introducing flow pulsatility and using the same model geometries. We have restricted our investigation to a well-defined single harmonic sinusoidal flow waveform with a superimposed steady component to reduce secondary flow effects associated with the detailed characteristics of the waveform and its reproduction. Rigid wall models are used and blood is assumed to be Newtonian. Although these conditions are not true *in vivo* it appears that the influence of wall compliance on the local hemodynamics is secondary compared to the effects of the overall geometry, inflow and outflow conditions and the transient behaviour of the flow. Liepsch and Moravec (1984) reported a reduction in wall shear stress magnitude and a damping of retrograde flow as a result of introducing wall compliance to their rigid wall arterial model. However Friedman et al. (1992) found no significant changes in the correlation of vascular disease to normalised wall shear by introducing wall compliance or a non-Newtonian fluid in their model. A study by Moore et al. (1994) comparing results from an *in vitro* glass model study and an *in vivo* study of the flow in the abdominal aorta, showed that the most important flow features present *in vivo*, such as skewed velocity profiles and flow reversal, where also present in the rigid wall model. In a later numerical investigation of flow in a compliant carotid artery model, Perktold and Rappitsch (1995) demonstrated that the global flow and shear stress patterns remain largely unchanged from the introduction of wall compliance. Limiting our investigation to a single harmonic sinusoidal flow waveform is also a deviation from the true physiological flow conditions. It allows however the dissociation of the fundamental effects of transient flow from the effects of patient or site-specific flow waveform characteristics on distal anastomotic hemodynamics. Although current blood flow investigations in models are moving towards more patient specific geometries and flow conditions (Perktold et al., 1998; Hughes et al., 1998; Moore et al., 1999), simplified model geometries can still help in better understanding the evolution and interaction of the complex flow structures that develop in bypass grafts and their relationship to various geometric parameters. In our investigation we use a combination of magnetic resonance imaging (MRI) experiments and numerical flow simulations to discuss the major features of the flow field. Wall shear stress direction maps and particle paths are used to illustrate the oscillatory motion of the stagnation point and the dynamic behaviour of the flow separation regions.

2. Materials and methods

2.1 Experimental Method

A 1.5 T (Signa Horizon LX: General Electric (GE) Medical Systems, Milwaukee, Wisconsin) MRI scanner was used to perform the experiments. A GE standard clinical cardiac-gated fast two-dimensional phase contrast pulse sequence was applied. The model was placed in the scanner with the axis of the host section aligned to the long axis of the magnet to avoid flow encoding misalignment errors. A dual 3-inch surface coil was used, and the flow phantom was placed in-between the two coil elements in a sandwich-like configuration. A field-of-view (FOV) of 7 cm × 7 cm was selected with a 256 × 256 image acquisition matrix, yielding an in-plane resolution of 0.273 mm. The echo time (TE) of the sequence was 5.5 ms and the repetition time (TR) was 16.7 ms. Only the axial velocity component was encoded using an aliasing velocity (V_{enc}) of 9 cm/s. This V_{enc} value was well below the numerically computed peak velocity in the flow region of interest (~35.5 cm/s). Although this choice of V_{enc} parameter led to velocity aliasing that had to be corrected offline, it extended the dynamic range of the measurement thus improving the precision of the experimental results (Papaharilaou et al., 2001a).

A 50 degrees flip angle was applied and a 2 mm slice was excited. Given that the data was extracted from a thin slice, 8 signal averages were employed to compensate for the inherently low signal to noise ratio (SNR) of the measurements. The temporal resolution of the scan was 66.8 ms that allowed for 25 phases to be reconstructed covering 90% of the waveform cycle. The acquisition duration was 15 minutes per slice location.

A computer controlled flow simulator (Quest Imaging Inc., London, Ontario) was used to generate the flow waveform for the experiments. A TTL pulse generated by the flow simulator at the start of each waveform cycle was used to trigger the MRI scanner. The circulating fluid was a 60-40% by volume distilled water-glycerol solution. To improve the SNR of the measurement a contrast agent (Gadolinium-DTPA, Omniscan, Nycomed) was introduced to the water-glycerol mixture to create a 0.75 mmol/L solution with a T_1 of ~60 ms at 1.5 T. The kinematic viscosity (ν) of the circulating fluid was measured using a capillary viscometer and was found to be $(3.4 \times 10^{-6} \pm 0.1)$ $m^2 s^{-1}$ at 20 ^oC. A sinusoidal flow waveform with a superimposed steady flow component was used with a value of the Reynolds number (Re) varying in the range of 62 to 437 with a mean value of 250. The Womersley parameter of the flow waveform was equal to 4.

The flow pump was calibrated for transient flow using a transit time flow meter (Transonic Systems Inc., Ithaca, New York). Flow was allowed to fully develop before entering the anastomosis of the model. Flow conditioning was achieved by including a sufficiently long straight tube section

upstream of the curved section of the model to meet the entrance length requirements for the flow according to the results of He and Ku (1994).

2.2 Computational Method

The computations were performed using a spectral/*hp* element algorithm (Sherwin and Karniadakis, 1996) to solve the three-dimensional time-dependent incompressible Navier-Stokes equations for unsteady flow. In this technique the solution domain is decomposed into tetrahedral subdomains or elements as is typical of standard finite element or finite volume discretisations. However, unlike the standard techniques, each tetrahedral region is represented by a polynomial expansion.

Convergence of the numerical solution may be achieved either by reducing the characteristic size (h) of an element or increasing the order (p) of the polynomial within each element. For smooth solutions the advantage of a p-type approach is that high accuracy for a given amount of computational work can be obtained efficiently from the point of view of accuracy for a given amount of computational effort (Sherwin and Karniadakis, 1996). The code has been validated extensively in steady and transient flows by comparisons with analytical and experimental results (Papaharilaou et al., 2001a&b; Sherwin et al., 2000; Sherwin et al., 1997; Doorly et al., 1997).

The computations were performed using the domains shown in Fig. 1 where the domain was subdivided into 1742 and 1941 tetrahedral elemental subdomains in the planar and non-planar models respectively. In constructing the computational domain a viscous layer of 0.1 D was imposed adjacent to the vessel walls in order to capture the oscillating boundary layer. Simulations were performed at polynomial orders of P = 4, 6 & 8 which correspond to approximate local degrees of freedom of 60 000, 150 000 and 300 000 per variable respectively. At the inflow boundary the exact Womersley solution was imposed whilst at outflow a fully developed pipe flow with the conditions of constant pressure and zero normal derivatives of velocity enforced. For the computations a time step of $\Delta t = 0.001$, normalized by mean inlet velocity per vessel diameter, was applied. The inflow conditions matched those prescribed for the experiments (2.1). Each polynomial order was computed for a minimum of three cycles and at P=8 the difference in the mean wall forces, integrated over the last two cycles, was less then 0.07 % of the mean inlet wall force.

The issues of numerically accuracy and mesh convergence have been addressed for steady flow in the paper by Sherwin et al. (2000). In this study the unsteady simulations were performed on the computational meshes used in the steady flow case but with a more refined discretisation where the order of the polynomial expansion within each element was increased from 6^{th} to 8^{th}. By this we have increased the local degrees of freedom within each element from 84 to 165 thereby doubling the resolution. It should be noted that a degree of freedom in the spectral/*hp* algorithm is not directly comparable with that in the standard linear finite element expansion basis which converges algebraically as compared to the exponential rate of convergence in the method used here. To establish mesh conver-

gence the procedure outlined in Sherwin et al. (2000) based on the evaluation of pressure and shear forces integrated over the walls at different polynomial expansion orders was followed. For the planar model simulation we know from symmetry that the *z*-component of force should tend to zero. In our computations the integral of the *z*-component of force using a 6^{th} order polynomial expansion was of the order of 10^{-3}. This value reduced to the order of 10^{-4} when the polynomial expansion was raised to 8^{th} order, indicating a good level of convergence in a mesh which has no specific symmetry.

A total of 32 CFD time slices covering the full waveform cycle were available and each slice was consistently interpolated at 8^{th} order accuracy onto a circular mesh with 50 radial and 100 azimuthal points. Experimental results were linearly interpolated onto a circular mesh of the same resolution. This operation did not smooth the MRI data since the inherent resolution of the experiment was less than that of the circular mesh selected. Finally velocity volume streamlines and shear vector surface streamlines where calculated at a post-processing stage using a commercial flow visualisation package (Tecplot v8.0, Amtec Engineering, Inc.).

2.3 Modified oscillatory shear index

To obtain a measure of the oscillatory motion of the wall shear stress vector we have calculated a modified oscillatory shear index (OSI) based on the definition of Ku et al. (1985) and the formulation introduced by Moore et al. (1999). As both shear vector magnitude and direction change with time in a continuous fashion we define OSI as:

$$OSI = \frac{\int_0^T w\left|\boldsymbol{\tau}\cdot\boldsymbol{n}_{mean}\right|dt}{\int_0^T \left|\boldsymbol{\tau}\cdot\boldsymbol{n}_{mean}\right|dt}$$

where $\boldsymbol{\tau}$ is the instantaneous wall shear stress, $\boldsymbol{n}_{mean}$ is the mean shear direction defined as $\boldsymbol{n}_{mean} = \int_0^T (\boldsymbol{\tau}/\|\boldsymbol{\tau}\|)dt$, where T is the period of the flow waveform and w is a weighting factor defined as $w = 0.5(1-\cos a)$, where a is the angle between $\boldsymbol{\tau}$ and $\boldsymbol{n}_{mean}$. This definition of the oscillatory shear index allows for the inclusion in the calculation of a continuous range of instantaneous shear vector angles with respect to the mean shear direction. The range of values for the modified index is 0<OSI<0.5 where 0 corresponds to unidirectional shear flow and 0.5 to the purely oscillatory shear case.

3. Results

3.1 MRI – CFD axial velocity comparison in the non-planar model

Figure 2 shows a comparison of the numerically computed and MRI measured axial velocity, normalised by the mean inlet velocity, in the non-planar model extracted at 0.25 D distal to the toe. Four points in the waveform cycle are shown. The combination of geometry and location were selected as the most challenging for both techniques based on the strength of the secondary flow and the complexity of the flow patterns present.

The direction of the flow in Fig. 2 should be interpreted as into the page with the left and right sides of the image corresponding to the bed and toe sides of the model respectively. The slice extraction location was dictated by the finite thickness (2 mm) of the MRI slice centred at 0.25 D downstream of the toe to avoid flow features proximal to the toe being introduced to the measurement. The overall agreement between MRI and computations is very good and within experimental error. By comparing the instantaneous root mean square differences between the computed and measured axial velocity profiles at three stations along the distal host vessel in the non-planar configuration, a spatially and temporally averaged rms error between 7.8 % and 11.5 % with respect to the spatially and temporally averaged velocity was calculated (Papaharilaou et al., 2001a). The crescent shaped velocity distribution and the presence of a separation region are the most prominent flow features at the toe. The bulk rotation in the velocity crescent associated with the swirling nature of the flow introduced by the upstream curvature in the graft is in phase with the flow rate.

As indicated in Fig. 2 flow separation at the toe first occurs during early flow acceleration with the flow separation region expanding until peak flow and gradually contracting thereafter until end deceleration where it disappears. A comparison of the MRI and CFD axial velocity profiles extracted along the vertical and horizontal centrelines at 0.25 D distal to the toe is shown in Fig. 3. The evolution of the separation region at the toe is clearly depicted on the toe wall side of the horizontal centreline profiles (y/D = - 0.5). Although the overall agreement is very good some mismatch between the computations and the experiments is evident at the near-wall region at the toe side (y/D = - 0.5). In that region the computations exhibit a highly non-linear profile, associated with retrograde flow, that probably exhausts the spatial resolution of the measurement. A direct result of the flow conditions in the recirculation region is a significant signal drop out associated with that region found in the experimental results. This drop in signal to noise ratio results primarily from the prolonged exposure of fluid particles to radio frequency pulses exciting the slice volume and suggests long residence times. The mismatch between the numerical and experimental results at the plateau of the profiles (z/D = 0) in the late acceleration phases of the cycle is a result of the combination of spatial displacement and acceleration artifacts (Papaharilaou et al., 2001a).

3.2 Axial velocity

Figure 4 shows a comparison of the spatial distribution of the axial velocity component at mid deceleration and at four stations along the host vessel in the two models. The out-of-plane inflow geometry breaks flow symmetry and establishes a bulk rotation of the velocity crescent that sets-up a Dean type flow in the graft vessel (Doorly et al., 1997). This rotation is evident in the host vessel and is dependent on the axial downstream distance from the toe. At the level of the toe on the bed wall we note the absence of retrograde flow in the non-planar model in contrast to the planar configuration. This is not separated flow and is caused by the oscillatory motion of the stagnation point discussed further in section 3.4. In the non-planar configuration there is a distal 0.25 D migration of the separation point as compared with the planar model. The separation region in the non-planar model reaches its full extent along the bed wall during late deceleration spanning a region between 0.25 D and 2 D distal to the toe. Furthermore in the non-planar model the peak axial velocity in the host vessel distal to the toe is reduced by 10 % on average as compared to the planar configuration. The effects of flow unsteadiness on the transient peri-anastomotic flow patterns although evident in both model configurations are more pronounced in the non-planar configuration.

Both models exhibit regions of flow separation with their temporal and spatial evolution dependent on the downstream distance from the toe. Flow separation first occurs during mid-acceleration with the separation point oscillating between the toe and 0.5 D distal to the toe in phase with the bulk flow. Apart from the distinctive clockwise displacement, looking down the vessel, of the separation zone in the non-planar model, its evolution is similar to the planar case. In the planar model the separation zone extents between the toe and approximately 1.7 D distal to the toe whereas in the non-planar model it extends between 0.25 D and 2 D distal to the toe. The size of the separation zone in both models is time dependent and peaks during late deceleration. Retrograde flow on the toe wall first appears at 0.5 D distal to the toe at mid-acceleration and gradually extends both distally and proximally during early deceleration until late deceleration. At end deceleration the adverse pressure gradient that causes flow separation has sufficiently weakened to allow full recovery of forward flow within the host vessel. Overall the introduction of out-of-plane curvature in the graft of the distal anastomosis causes a distal shift of the most proximal location of the separation point and a change in the spatial distribution of the separation region along the toe wall of the host artery as compared to the planar configuration.

3.3 Secondary flow

A comparison of the computed normalized horizontal–v velocity and the cross-flow streamlines in the two model geometries is shown in Fig. 5. Flow symmetry is preserved in the planar model al-

though not explicitly prescribed in the solution. The magnitude of the strongest (horizontal v-velocity) cross flow component is inversely related to the downstream distance from the toe. It drops steeply in the region between 0 D and 2 D downstream of the toe and more gradually further downstream. In the planar model we note the presence of two symmetric counter-rotating vortices in the transverse plane. These Dean type vortices account for the clockwise and counterclockwise motion of fluid particles in the upper and lower recirculation regions respectively. On the toe wall at 4 D downstream of the toe two weak vortices rotating against the main vortices appear. These vortices are probably caused by the delayed response of viscous effects on the axial separated flow just downstream of the toe.

The out-of-plane curvature introduced in the non-planar configuration breaks flow symmetry and causes a 10 % reduction in the peak cross flow magnitude at the toe as compared to the planar configuration. Although two counter-rotating cells can still be identified at the toe as in the planar case, the upper cell is significantly stronger than the lower one. As a result a strong clockwise vortex with its core at the top of the cross section dominates and the weaker secondary counterclockwise vortex is constrained spatially at the lower part of the cross section. At 2 D downstream of the toe the core of the dominant vortex has rotated clockwise by 90 degrees and has generated a weak secondary co-rotating vortex in the process. The core of the weaker vortex appears displaced towards the vessel axis. By 4 D distal to the toe the weaker vortices have dissipated and a single vortex remains.

3.4 Wall Shear Stress

The wall shear stress maps shown in Figs. 6 and 7 should be interpreted so that the horizontal axis represents distance along the host vessel and the vertical axis represents the circumferential distance along the wall of the host vessel. The orientation of the map has been selected so that the bed region appears at the centre. Wall shear stress has been normalized with respect to the wall shear stress of the Hagen-Poiseuille flow within a straight pipe of the same diameter and with Re = 250. Irregularities seen in the shape of the wall shear stress contour lines along the horizontal centerline in the non-planar model are due to velocity gradient discontinuities across mesh element boundaries.

Figure 6 shows a comparison of the numerically computed steady and pulsatile mean wall shear stress magnitude distribution in the planar and non-planar models. Also shown is a comparison of the numerically computed pulsatile mean axial component of wall shear stress in the two models where regions of negative shear are clearly marked by zero axial shear contours. There is a 10 % increase in the temporally averaged peak wall shear stress in pulsatile flow as compared to steady flow. The asymmetry of the flow in the non-planar model leads to an increased concentration of high shear levels at the lower half of the shear map. The location of the peak wall shear stress magnitude has been displaced proximally and away from the bed centerline in the non-planar model at 0.5 D as compared to 0.8 D downstream of the toe in the planar case. There is also a 10 % reduction in the peak wall

shear stress magnitude in the non-planar model as compared to the planar configuration. Overall, a more uniform distribution of wall shear stress results from the introduction of the upstream out-of-plane curvature.

Figure 7 shows a comparison of the numerically computed normalized wall shear stress magnitude in the planar and non-planar models at four points in the flow cycle with wall shear vector surface streamlines superimposed. Points where shear streamlines converge to or diverge from or are of particular interest as they indicate separation and reattachment (stagnation) points respectively. A characteristic feature in both wall shear stress maps is a region of low shear at the toe level on the bed wall of the anastomosis associated with a stagnation point. The proximity of this low shear zone to a high shear region creates steep spatial gradients of shear that are accentuated in the non-planar model by the presence of an additional high shear cell proximal to the low shear area.

The magnitude of wall shear stress in the region proximal to the heel is one to three orders of magnitude less than the temporal mean shear stress at the graft inlet. This is due to the limited mass flux through the heel in the occluded host section. Note the proximal displacement of the minimum wall shear stress contour (0.002) in the non-planar model indicating elevated shear stress levels in the occluded host vessel region as compared to the planar configuration. In terms of the dynamic behavior of the wall shear stress distribution we note a 30 % drop in the peak wall shear stress magnitude in the non-planar model at mid deceleration as compared to the planar configuration with subsequent effects on the magnitude of the associated spatial gradients of shear.

An important difference between the two geometries is related to the location and motion of the stagnation point. By tracking the excursion of the stagnation point throughout the flow cycle we identified significant differences in both amplitude and direction of its oscillatory motion between the two models (Fig. 7). In the planar configuration the stagnation point oscillates along the symmetry line on the bed and between 0.7 D proximal to the toe at early acceleration and 0.1 D distal to the toe at mid deceleration. In the non-planar case the stagnation point oscillates about a center that is located off the symmetry plane intersection with the host artery bed wall, and following a parabolic path with a 0.7 D longitudinal and 0.5 D transverse excursion. We should note that in both configurations we the stagnation point disappears between end acceleration and early acceleration. In the non-planar model during early acceleration a reattachment line initially forms (Fig. 7) becoming a point during the following phase in the cycle.

On the wall shear streamline maps points of shear direction reversal are of particular interest as they highlight flow separation zones. The location of the reattachment point can be readily identified at the top and bottom of the shear direction map of the planar model at mid deceleration. In the non-planar configuration and at mid deceleration the separation zone is shifted away from the toe wall towards the bed wall and extends along a line that is oblique to the vessel axis. This behavior is associated with the bulk flow rotation forced by the upstream curvature in the graft.

3.4.1 Oscillatory shear index

Figure 8 shows a comparison of the oscillatory shear index distribution in the planar and non-planar configurations calculated applying the OSI definition introduced in section 2.3 and the definition of Moore et al. (1999). The OSI calculations were performed at a post processing stage using the computed shear distribution in the unfolded host vessel. A threshold of 5 % of the mean Poiseuille flow wall shear stress magnitude was applied to exclude very low signal to noise shear data (primarily from the occluded proximal host region) from the oscillatory shear index calculation. The irregularities in some of the contours in Fig. 8 are indicative of the difficulty in resolving this flow index. Distinct regions of elevated oscillatory shear can be identified in both models. One such region encapsulates the spatial temporal mean location of the stagnation point on the bed of the planar anastomosis. Another region of elevated oscillatory shear located on the toe wall of the host vessel exhibits a peak at 0.8 D downstream of the toe and extends between the toe and 2 D downstream of the toe. This region is spatially associated with the flow separation zone on the toe wall depicted in Figs. 4 and 7.

In the non-planar model regions of elevated oscillatory shear are also spatially associated with the separation zone and the stagnation point. We note however that the region of elevated oscillatory shear does not stretch along the path followed by the stagnation point. This can be explained by the spatio-temporal concentration of the motion of the stagnation point that accounts for the filtering effect exhibited by the oscillatory shear index localisation. Regions of elevated shear not accounted for by the stagnation point dynamics are associated with a secondary flow separation proximal to the toe on the bed of the anastomotic wall. This flow separation can be identified on the shear direction maps (Fig. 7) during peak flow and mid deceleration as a point of shear vector streamtrace convergence. This secondary separation is associated with the complex flow vortices that develop in the anastomotic junction. The spatial extent of the elevated oscillatory shear regions is reduced in the non-planar model and as compared to the planar configuration. Moreover, in the non-planar model, and for OSI values above 0.1, the mean oscillatory shear was reduced by 22 % as compared to the planar configuration.

Figure 9 shows a close-up of the oscillatory shear distribution in both model configurations in the vicinity of the stagnation point trace that is also shown. Several points are worth noting. There is significant temporal concentration of the stagnation point excursion in both models although more pronounced in the non-planar configuration. This region of concentrated stagnation point movement corresponds spatially with a peak in the oscillatory shear magnitude. Most of this motion occurs during early acceleration with the stagnation point positioned most proximally during the first acceleration phase.

The comparison of the oscillatory shear distribution obtained by the definition of Moore et al. (1999) and the modified definition proposed here shows, as expected, a very similar distribution pattern in both cases. However, a significantly reduced spatial extent and less uniform distribution of os-

cillatory shear are evident in the existing definition as compared to the modified OSI definition proposed.

3.5 Flow in the proximal non-planar host vessel

Figure 10 shows the flow behaviour at the anastomotic junction. Figs. 10a and b show an axial velocity contour map extracted along the z = -0.3 D plane at mid acceleration (a) and early deceleration (b). Vectors and streamtraces of the in-plane velocity components are also plotted. Note the formation of a recirculation region, which varies in spatial extent and configuration throughout the cycle. In the x-y plane, the recirculation appears as a vortex, and the streamlines in this plane show fluid particles that enter the occluded part of the host vessel are swept back into the main flow stream by the vortex and are convected downstream in the host vessel. However the vortical structure is three-dimensional, and varies both in strength and configuration. Turning to Figs. 10c and d, at mid-acceleration an almost symmetrical pair of vortex cores are found which transport flow out of the proximal portion, whereas at mid deceleration, a single strong vortex is generated by the decelerating flow and draws flow out of the recirculation region limiting the spatial extent of the flow reversal. The instantaneous Reynolds number is (Re=200) for plots (a) and (c) and (Re=250) for plots (b) and (d); so although these do differ to some extent, the flow features are radically altered indicating the profound effect of the flow unsteadiness.

The structure of the vortex is complex but some insight can be had from examining the paths of particles released into the flow frozen in the cycle at the mid-deceleration point (Fig. 10e). The trajectory of fluid particles released on the bed wall of the non-planar model upstream and downstream of the three-dimensional separation point marked by converging wall shear streamlines and elevated oscillatory shear can be seen in Fig. 10e. At x/D = -1.1 on the bed wall fluid particles arriving from both directions converge and are pulled swiftly off the wall to join the strong clockwise vortex forming at the centre of the lumen. Time integration markers are equally spaced in time and show the temporal evolution of the particles released. Released fluid particles initially move slowly along the wall and upstream towards the occluded section of the proximal host vessel. As they reach the level of the heel they experience the strong in-plane force associated with the vortex located near the axis of the vessel and are drawn towards its core. As particles enter the vortex core they attain a swirling motion and are convected downstream where they rejoin the main flow stream and swiftly gain momentum. Also shown in Fig 10e is the trajectory of a particle released in the recirculation region (a region of elevated OSI) at the toe wall and just distal to the toe. Note the initial very slow upstream motion of the particle within the separation region and the swift change of direction as it negotiates the separation boundary.

4. Discussion

The aim of this investigation is to demonstrate the fundamental effects of flow pulsatility on the flow field in two geometric configurations of a distal end-to-side anastomosis. As discussed in the introduction, the flow conditions are somewhat idealized (Newtonian fluid assumed, rigid wall models used, single harmonic flow waveform applied) as the primary effect we wish to identify is that of the geometry.

The introduction of time-varying flow in the investigation on the effects of out-of plane graft curvature in a distal end-to-side anastomosis produced several interesting results. Although the gross features of the flow were similar to those found in the steady flow investigation of Sherwin et al. (2000), a number of important distinctive features are introduced. One such feature is the extensive flow separation observed on the toe wall just downstream of the toe in both model configurations. Low shear magnitude and long residence times associated with flow separation regions are hemodynamic conditions shown to promote the development of early vessel wall disease processes. In a detail investigation of flow separation in the planar anastomosis for steady flow Ethier et al. (2000) reported no axial flow separation for $Re<250$, in agreement with the result of Sherwin et al. (2000), and a single separation region on the toe wall and slightly downstream of the toe for Re between 250 and 450. Interestingly, for $Re>450$ they reported the formation of a second separation zone 1.3 diameters downstream of the toe. The unsteady flow results reported here where the Reynolds number varies between 62 and 437 show only a single axial flow separation region in both model configurations. The temporal and spatial evolution of this separation region is strongly influenced by the graft geometry and is coupled to the flow oscillation.

The 10% reduction in the peak magnitude of the time averaged wall shear stress in the non-planar model as compared to the planar configuration found here is in line with the steady flow result of Sherwin et al. (2000). The dynamic behavior of the stagnation point on the bed of the anastomosis is of particular interest as it may assist in predicting the localization of vessel wall disease. While factors such as high shear magnitude and long exposure time may lead to platelet activation, forces acting in the direction of the vessel wall, as those found in the vicinity of a reattachment point, are necessary to carry activated platelets to the endothelium. The adhesion and aggregation process of activated platelets convected to the wall in the locality of the stagnation point is augmented by the low shear environment of the flow separation region (Wurzinger et al., 1983; Blasberg et al., 1983). It has been shown (Wurzinger et al. 1983; Karino and Goldsmith, 1984) *in vitro* that regions in the neighborhood of the stagnation point are prone to thrombus formation, as platelets tend to strongly adhere to the wall at these sites. It has also been shown for steady flow in perfusion models (Pritchard et al., 1995) that blood monocyte adhesion to the vessel wall is inversely correlated to wall shear stress and is strongly influenced by the magnitude of in-plane flow and the presence of flow separation. In addition a recent investigation by Hinds et al. (2001) with both steady and pulsatile flow in a three dimensional perfusion model showed that blood monocyte adhesion was significantly higher in the locality of the flow separation region as compared to the post reattachment and pre-separation regions. They also found

that flow pulsatility significantly altered monocyte adhesion patterns and introduced an overall more uniform adherent cell distribution. Therefore, the significant differences found in this study in the pattern of the oscillatory excursion of the stagnation point between the two model configurations suggests a strong influence of out-of plane graft curvature in the distribution of sites on the vessel wall exposed to unfavorable hemodynamic conditions.

The significant changes in the spatial distribution of the separation zone associated with the introduction of out-of-plane curvature in the graft highlights the strong influence of the three-dimensional character of the anastomosis on the flow behavior in the native vessel. If blood monocytes tend to adhere more readily to the endothelium at regions of low shear stress and flow separation thus promoting the development of vessel wall disease, then based on the results of this study a reduction of the spatial extent of early wall lesions in the non-planar model as compared to the planar configuration might be expected. Furthermore, if a correlation between regions of elevated oscillatory shear and intimal thickening exists, as shown by Ku et al. (1985) in the carotid bifurcation, then the 22 % reduction in mean oscillatory shear found in the non-planar model as compared to the planar configuration would imply a corresponding reduction in the spatial extent of wall regions exposed to physiologically unfavorable flow conditions.

The flow behaviour in the occluded section of the host vessel is of considerable interest as it is associated with long residence times a flow condition known to promote clot formation. Thrombotic wall lesions initiated in the occluded part of the host vessel may proliferate distally penetrating the perianastomotic flow conduit and augment restenosis. Sherwin et al. (2000) found in steady flow an 80 % increase in the mass flux through the heel in the non-planar model as compared to the planar configuration. In pulsatile flow we have found an overall increase in the wall shear stress magnitude in the occluded section of the host vessel as a result of the introduction of upstream out-of-plane curvature in the geometry. This can be attributed to the development of a strong vortex at the heel directed downstream that sweeps particles, separated from the main flow on the bed, which enter the occluded section of the host vessel back into the main stream.

In the controlled conditions of an idealized anastomosis model it was possible to characterize flow features such as flow separation, and stagnation and associate them with specific geometric parameters. It is shown that the introduction of out-of-plane curvature in the graft strongly influences perianastomotic flow and is thus expected to affect the localization of vessel wall disease. It would therefore be of interest to extend this investigation to assess the sensitivity of the flow to the degree of out-of-plane curvature.

Although gross geometric features are considered as the most influential factors in vascular hemodynamics it is the combined effect of gross and detailed features of geometry acting in conjunction with factors such as flow pulsatility and vessel wall mechanics that accounts for the variability in the localization and extent of lesions in revascularised vessels *in vivo*. Therefore, a series of studies incrementally incorporating flow and geometric features closer to the true *in vivo* hemodynamic condi-

tions in arterial bypass grafts are necessary in order to assess the range and importance of the effects of natural geometric and flow waveform variability between individuals on perianastomotic flow patterns.

Acknowledgements

The authors will like to acknowledge financial support for this work by the BUPA, the Garfield Weston Foundation, the University of London Academic Trust Funds, the 'Lilian Voudouri' Foundation of Greece and the Clothworkers' Foundation. We will also like to extend our thanks to Dr. Joaquim Peiro for his invaluable assistance in the generation of the computational mesh and Prof. Colin Caro for setting the ground for this study with his inspirational ideas. We also extend our thanks to the MagNET group for the computer controlled flow pump. The computations were performed on the Biomedical Visualisation Origin 2000 system and on the CSAR Cray T3E under the turbulence consortium.

References

Asakura, T., Karino, T., 1990. Flow patterns and spatial distribution of atherosclerotic lesions in human coronary arteries. Circ. Res. 66, 1045-1066.

Bassiouny, H.S., White, S., Glagov, S., Choi, E., Giddens, D.P., Zarins, C.K., 1992. Anastomotic intimal hyperplasia: mechanical injury or flow induced. J Vasc Surg 15, 708-716.

Blasberg, P., Wurzinger, L.J., Scmhid-Schonbein, H. 1983. Microrheology of thrombocyte deposition: effect of stimulation flow direction, and red cells. In Fluid dynamics as a localising factor for atherosclerosis. Edited by Schettler, G., Nerem, R.M., Schmid-Schonbein, H., Morl H., Diehm, C. pp. 91-101. Springer, Berlin.

Bryan, A.J., Angelini, G.D., 1994. The biology of saphenous vein graft occlusion: etiology and strategies for prevention. Curr. Opin. Cardiol. 9, 641-649.

Caro, C.G., Doorly, D.J., Tarnawsk, M., Scott, K.T., Long, Q., Dumoulin, C.L., 1996. Non-Planar curvature and branching of arteries and non-planar-type flow. Proc. R. Soc. Lond. A, 452, 185-197.

Cheshire, N.J., and Wolfe, J.H., 1993. Infrainguinal graft surveillance: a biased overview. Semin Vasc Surg 6, 143-149.

Davies, P., 1995. Flow mediated endothelial mechanotransduction. Physiol. Rev. 75, 519-560.

Ding, Z., Friedman, M., 1997. Variability in planarity of the aortic bifurcation measured from Magnetic Resonance Images. In Proceedings of the Bioengineering Conference, ASME BED-Vol. 35.

Doorly, D.J., Peiro, J., Sherwin, S.J., Shah, O., Caro, C.G., Tarnawski, M., MacLean, M., Dumoulin, C., Axel, L., 1997. Helix and model graft flows: MRI measurement and CFD simulations. In Proceedings of the ASME FED meeting. ASME Paper No. FEDSM-97-3423.

Ethier, C.R., Steinman, D.A., Zhang, X., Karpik, S.R., Ohja, M., 1998. Flow waveform effects on end-to-side anastomotic flow-patterns. J. Biomech. 31, 609-617.

Ethier, C.R., Prakash, S., Steinman, D.A., Leask, R.L., Couch G.G., Ohja M., 2000. Steady flow separation patterns in a 45 degree junction. J. Fluid Mech. 411, 1-38.

Friedman, M.H., Bargeron, C.B., Deters, O.J., Hutchins, G.K., Mark, F.F., 1987. Correlation between wall shear and intimal thickness at a coronary artery branch. Atherosclerosis 68, 27-33.

Friedman, M.H., Bargeron, C.B., Duncan, D.D., Hutchins, G.K., Mark, F.F., 1992. Effects of arterial compliance and non-newtonian rheology on correlations between intimal thickness and wall shear. J. Biomech. Eng. 114, 317-320.

He, X., Ku, D.N., 1994. Unsteady entrance flow development in a straight tube. J. Biomech. Eng. 116, 355-360.

Henry, F.S., Collins, M.W., Hughes, P.E., How,T.V., 1996. Numerical investigation of steady flow in proximal and distal end-to-side anastomoses. J. Biomech. Eng. 118, 302-310.

Hinds, M.T., Park Y.J., Jones S.A., Giddens D.P., Avevriadou B.R., 2001. Local hemodynamics affect monocytic cell adhesion to a three-dimensional flow model coated with E-selectin. J. Biomech. 34, 95-103.

Hofer, M., Rappitsch, G., Perktold, K., Trubel, W., Schima, H., 1996. Numerical study of wall mechanics and fluid dynamics in end-to-side anastomoses and correlation to intimal hyperplasia. J. Biomech. 29, 1297-1308.

Hughes, T.H., Taylor, C., Zarins, C., 1998. Finite element modelling of blood flow in arteries. Comp. Meth. Appl. Mech. Eng., 158, 155-196.

Karino, T., Goldsmith, H.L., 1984. Role of blood cell-wall interactions in thrombogenesis and atherogenesis: a microrheological study. Biorheology. 21, 587-601.

Ku, D.N., Giddens, D., 1983. Pulsatile flow in a model carotid bifurcation. Atherosclerosis 3, 31-39.

Lei, M., Kleinstreuer, C., Archie, J.P., 1997. Heamodynamic simulations and computer aided designs of graft-artery junctions. J. Biomech. Eng. 119, 343-348.

Lei, M., Giddens, D.P., Jones., S.A., Loth F., Bassiouny, H., 2001. Pulsatile flow in an end-to-side vascular model: comparison of computations with experimental data. J. Biomech. Eng. 123, 80-87.

Leipsch, D., Moravec, S., 1984. Pulsatile flow of non-newtonian fluid in distensible models of human arteries. Biorheology 21, 571-586.

Moore, J.E. Jr., Maiser, S.E., Ku, D.N., Boesiger, P., 1994. Haemodynamics in the abdominal aorta: a comparison of *in vitro* and *in vivo* measurements. J. Appl. Physiol. 76, 1520-1527.

Moore, J.A., Steinman, D.A., Prakash, S., Johnston, K.W., and Ethier, C.R., 1999. A numerical study of blood flow patterns in anatomically realistic and simplified end-to-side anastomoses. J. Biomech Eng. 121, 265-272

Ohja, M., Ethier, C.R., Johnston, K.W., Cobbold, R.S., 1990. Steady and pulsatile flow fields in an end-to-side arterial anastomosis model. J. Vasc. Surg. 12, 747-753.

Ohja, M., 1993. Spatial and temporal variations of wall shear stress within an end-to-side arterial anastomosis model. J Biomech. 26, 1377-1388.

Papaharilaou, Y., Doorly, D.J., Sherwin., S.J., 2001. Assessing the accuracy of two-dimensional phase-contrast MRI measurements of complex unsteady flows. J. Magn. Reson. Imaging 14, 714-723.

Papaharilaou, Y., Doorly, D.J., Sherwin, S.J, Peiro J., Anderson J., Sanghera, B.,Watkins, N., Caro, C.G., 2001. Combined MRI and computational fluid dynamics detailed investigation of flow in a realistic coronary artery bypass graft model. In: Proc. of the 9th ISMRM-ESMRMB meeting, Glasgow, p. 379.

Pritchard, W.F., Davies P.F., Derafshi, Z., Polacek, D.C., Tsao, R., Dull, R.O., Jones, S.A., Giddens, D.P., 1995. Effects of wall shear stress and fluid recirculation on the localisation of circulating monocytes in a three-dimensional flow model. J. Biomech. 28, 1459-1469.

Perktold, K., Rappitsch, G., 1995. Computer simulation of local blood flow and vessel mechanics in a compliant carotid artery bifurcation model. J. Biomech. 28, 845-856.

Perktold, K., Hofer, M., Rappitsch, G., Loew, M., Kuban, B.D., Friedman, M.H. 1998. Validated computation of physiologic flow in a realistic coronary artery branch. J. Biomech. 31, 217-228.

Sherwin, S., Shah, O., Doorly, D.J., et al., 1997. Visualisation and computational study of model planar and non-planar end-to-side arterial bypass grafts. Physiological Society Abstracts Plymouth.

Sherwin, S.J., Karniadakis, G., 1996. Tetrahedral *hp* finite elements: algorithms and flow simulations. Journal of Computational Physics 124, 14-45.

Sherwin, S.J., Shah, O., Doorly, D.J., Peiro, J., Papaharilaou, Y., Watkins, N., Caro, C.G., Dumoulin, C.L., 2000. The influence of out-of-plane geometry on the flow within a distal end-to side anastomosis. J. Biomech. Eng. 122, 86-95.

Sottiurai, V.S., Yao, J.S., Batson, R.C., Sue, S.L., Jones, R., Nakamura, Y.A., 1989. Distal anastomotic intimal hyperplasia: histopathologic character and biogenesis. Ann. Vasc. Surg. 3, 26-33.

Steinman, D.A., Frayne, R., Zhang, X.D., Rutt, B.K., Ethier, C.R., 1996. MR measurement and numerical simulation of steady flow in an end-to-side anastomosis model. J. Biomechanics 29, 537-542.

White, S.S., Zarins, C.K., Giddens, D.P., Bassiouny, H., Loth, F., Jones, S.A., Glagov, S., 1993. Hemodynamics patterns in two models of end-to-side vascular graft anastomosis: effects of pulsatility, flow division, Reynolds numbers and hood length. J. Biomech. Eng. 115, 104-111.

Wurzinger, L.J., Opitz, R., Blasberg, H., Eschweiler, H., Schmid-Schonbein, H., 1983. The role of hydrodynamic forces in platelet activation and thrombotic events: the effects of shear stress of short duration. In: Fluid dynamics as a localising factor for atherosclerosis. Edited by Schettler, G., Nerem, R.M., Schmid-Schonbein, H., Morl H., Diehm, C., pp 91-101. Springer, Berlin.

Xu, X.Y., Long, Q., Bourne, M., Griffith, T.M., 1999. Effect of non-planarity on local blood flow patterns at human aortic bifurcations. In: Proc. of the Euromech Coll 389, Graz.

Yamamoto, T., Tanaka, H., Jones, C.J., Lever, J.M., Parker, K.H., Kimura, A., Hiramatsu, O., Ogasawara, Y., Tsujioka, K, Caro, C.G., Kajiya, F. 1992. Blood velocity profiles in the origin of the canine renal artery and their relevance in the localisation and development of atherosclerosis. Atheroscler. Thromb. 12, 626-632.

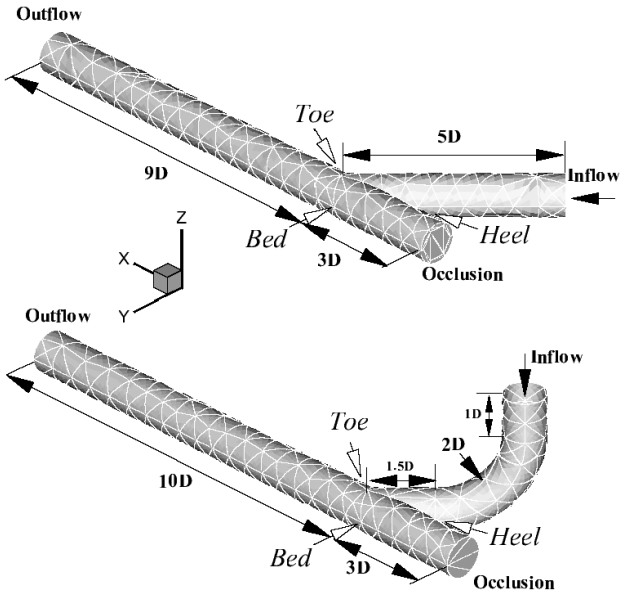

Figure 1. Model geometries of a distal 45 deg end-to-side anastomosis: planar (top) and non-planar (bottom) with numerical grid marked on vessel surfaces. All dimensions shown are scaled with vessel diameter.

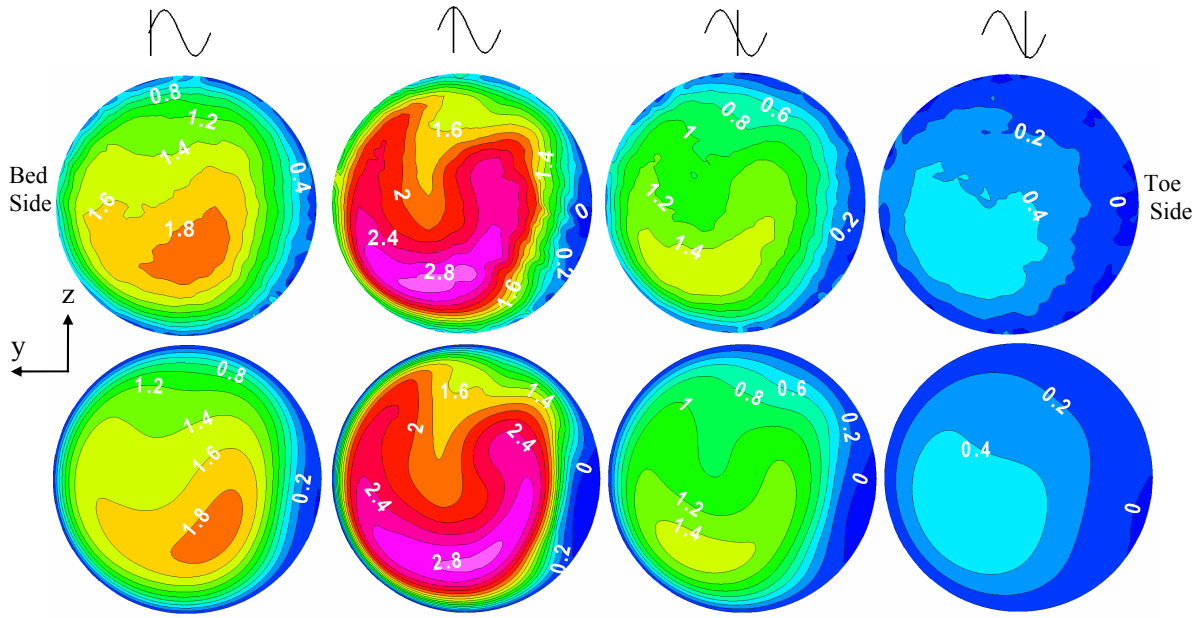

Figure 2. Comparison of MRI measured (top) and numerically computed (bottom) axial velocity, normalised by mean flow rate per unit area, at 0.25D downstream of the toe and (from left to right) at approximately mid acceleration, peak flow, mid deceleration and late deceleration in the non-planar geometry. Cross sections plotted with bed wall on the left and toe wall on the right.

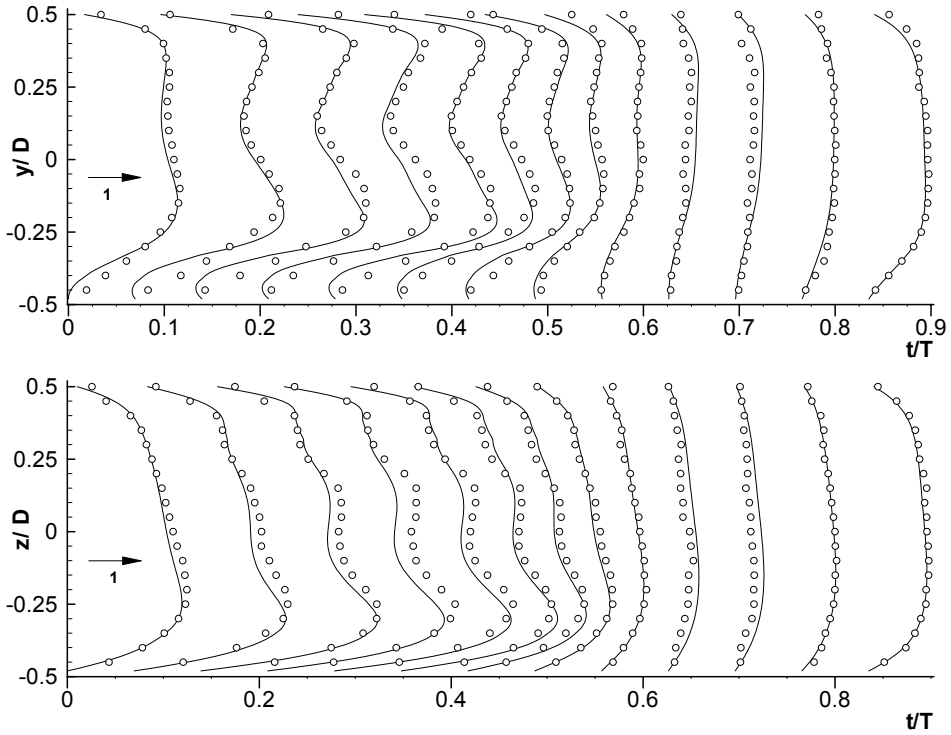

Figure 3. Comparison of the normalized axial velocity profiles from MRI (symbols) and CFD (solid line) at the toe in the non-planar geometry. Profiles are extracted along the constant *z* centerline (top) and the constant *y* centerline (bottom). A non-dimensional (*t*/*T*) time axis is used and 90 % of the waveform cycle is shown. The center of the cross section is at $y = 0$, $z = 0$. The toe lies at $y/D = -0.5$ and the bed at $y/D = 0.5$. Peak systole corresponds to t/T = 0.25.

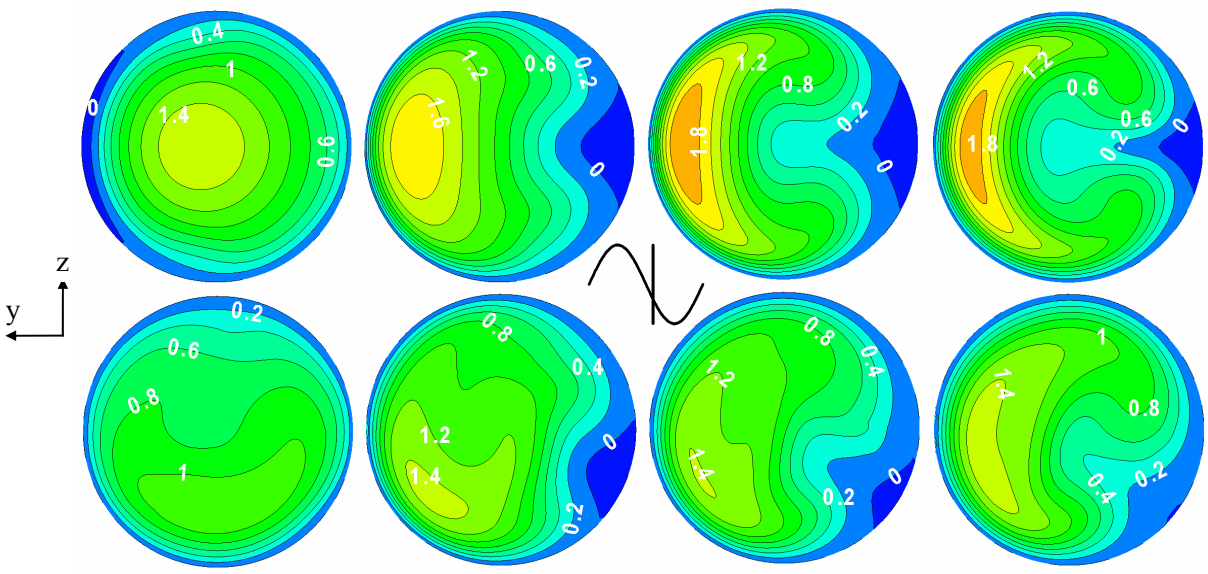

Figure 4. Numerically computed normalised axial velocity contour plots extracted (from left to right) at toe, 0.5D, 1D and 1.5D downstream of the toe from the planar (top) and non-planar (bottom) models just after mid-deceleration.

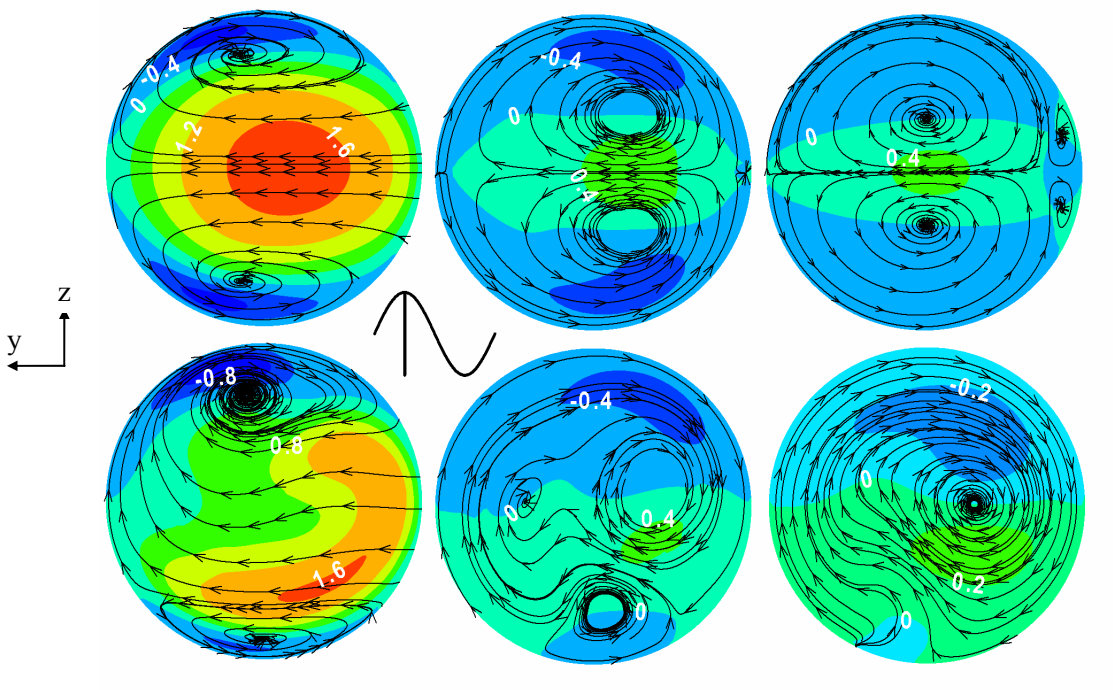

Figure 5. Comparison of numerically computed normalised horizontal v-cross flow velocity and cross flow streamlines in the planar (top) and non-planar (bottom) geometries at peak flow. Velocities extracted and streamlines calculated at the 'toe' (left), 2D distal to the 'toe' (centre) and 4D distal to the 'toe' (right).

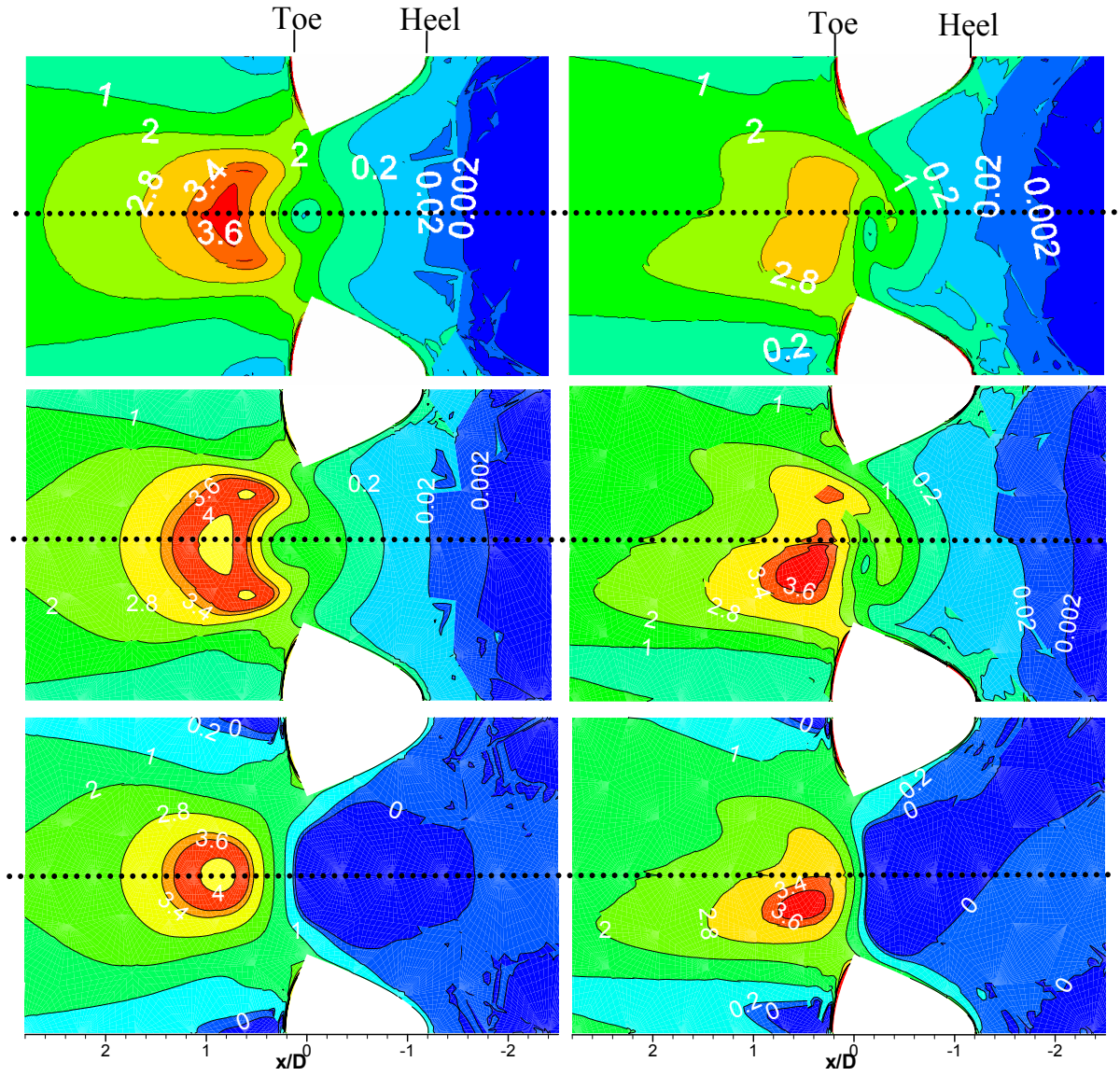

Figure 6. Comparison of numerically computed steady flow wall shear stress magnitude (top), mean pulsatile flow wall shear stress magnitude (middle) and mean pulsatile flow axial wall shear stress (bottom), normalized with the mean Poiseuille flow wall shear stress, in the unfolded planar (left) and non-planar (right) models. Dotted line plotted along the bed of the host vessel.

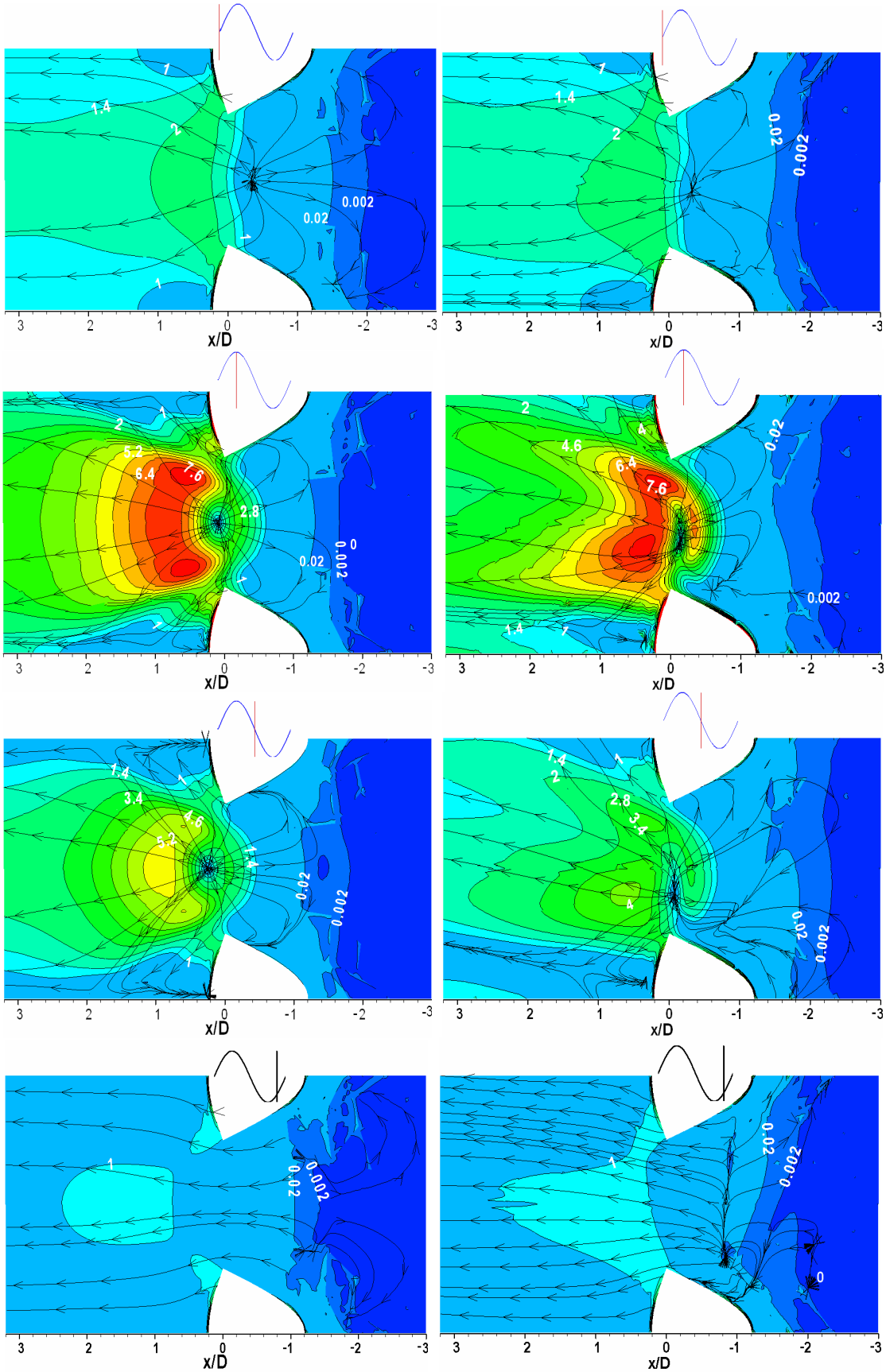

Figure 7. A comparison of numerically computed normalized wall shear stress magnitude, in the unfolded planar (left) and non-planar (right) models. Shear stress maps are shown at mid acceleration (top), at peak flow and mid deceleration (middle) and early acceleration (bottom). Stream traces of the wall shear vector are also shown.

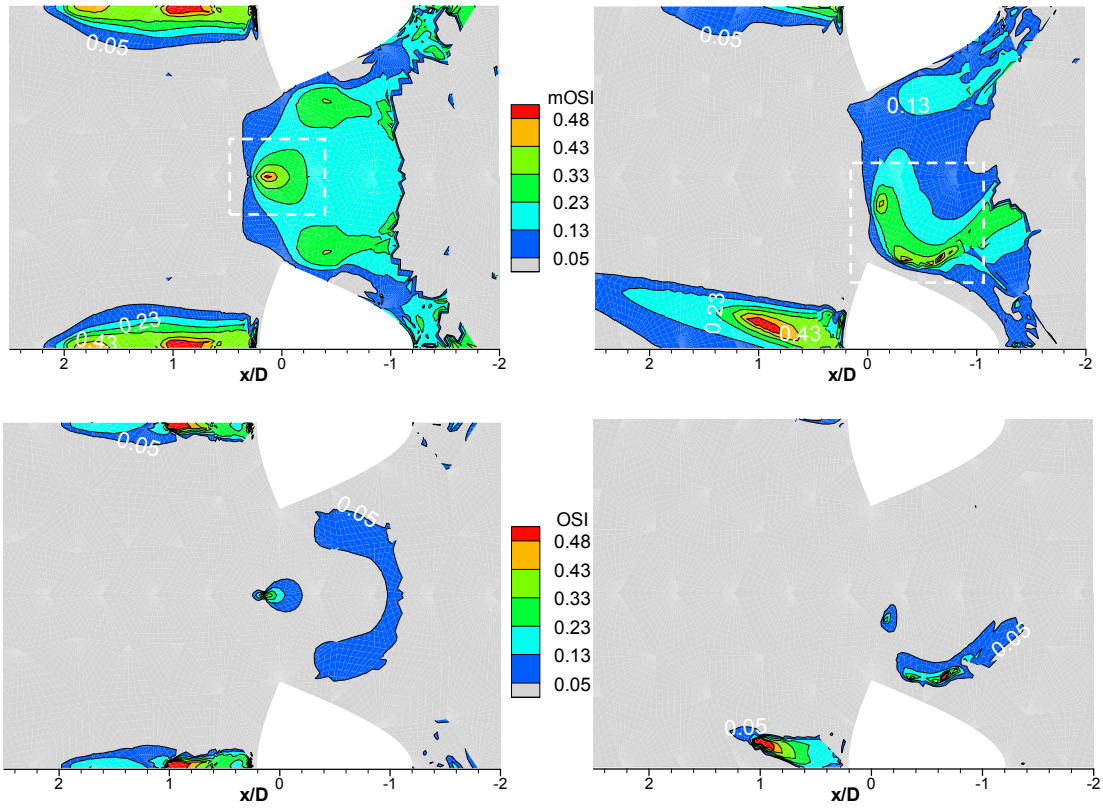

Figure 8. Comparison of the numerically computed modified (top) and original (bottom) oscillatory shear index in the unfolded planar (left) and non-planar (right) models. Regions enclosed by dashed lines are shown in close-up view in Fig. 9.

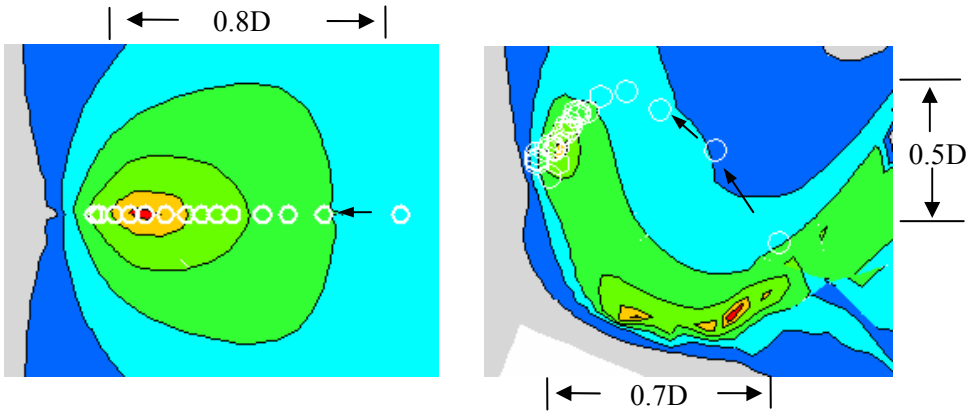

Figure 9. Comparison of the stagnation point excursion on the wall of the unfolded host vessel in the planar (left) and non-planar (right) anastomosis. Symbols are superimposed on close-up of the corresponding oscillatory shear index map region and are equally spaced in time. Right most symbols correspond to early acceleration and arrows indicate the direction of motion of the stagnation point.

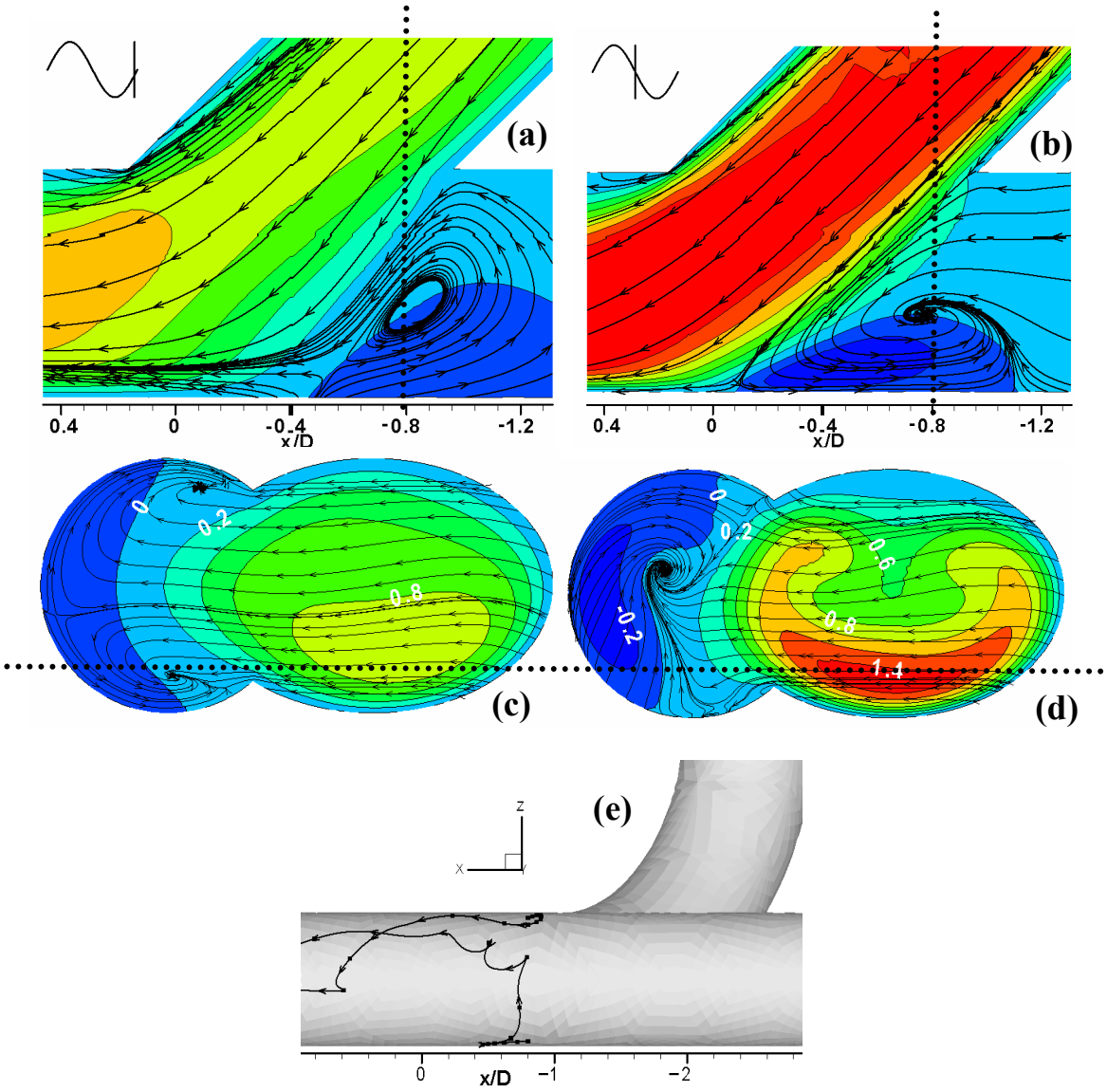

Figure 10. Flow patterns in the graft-host artery junction of the non-planar anastomosis. Streamtraces and vector plots at an x-y plane extracted at z=-0.3D at (a) approximately mid-acceleration and mid-deceleration (b). Streamtraces superimposed on axial velocity contours extracted at 1D proximal to the toe (c-d) at mid-acceleration (c) and mid-deceleration (d). Dotted line indicates level of slice extraction plane shown in (a) and (b). Also shown trajectories of fluid particles released at points within the elevated oscillatory shear region 1D proximal to the toe at mid-deceleration (e).